EES Catalysis

PAPER

View Article Online
View Journal

Cite this: DOI: 10.1039/d5ey00279f

Activity and degradation of Pt–Co and Pt–Ni alloy catalysts for application in high-temperature PEM fuel cells

Jan Dismas Buriánek, [a] Martin Prokop, [a] Tomas Bystron, *[a] Martin Veselý, [b] Lukáš Koláčný, [b] Bruna Ferreira Gomes, [c] Carlos Manuel Silva Lobo, [c] Matija Gatalo, [de] Luka Pavko, [de] Nejc Hodnik, [d] Martin Paidar, [a] Christina Roth, [c] Miran Gaberscek [d] and Karel Bouzek [a]

In the emerging hydrogen energy economy, proton-exchange membrane fuel cells (PEMFCs) serve as a key enabling technology, yet their cost is among other things dominated by platinum group metals-based cathode catalysts. This paper is focused on investigation of intermetallic Pt–Co and Pt–Ni nanoparticles supported on carbon (Ketjen black, reduced graphene oxide) as low-Pt-load candidates for high-temperature PEMFCs (HT-PEMFCs) operated at elevated temperature ~180 °C in the presence of concentrated phosphoric acid. Catalytic activity toward the oxygen reduction reaction (ORR) was quantified by rotating electrode measurements (exchange current densities, Tafel slopes), and stability was probed by leaching in 97.6 wt% H_3PO_4 at 180 °C followed by post-exposure characterisation. A suite of techniques – XAS, XRD, TEM/EDS, XRF, Raman spectroscopy and ICP-OES – was used to study changes in composition and structure during degradation. All alloy catalysts showed in $HClO_4$ at 25 °C higher ORR activity than commercial Pt/C. However, exposure to concentrated H_3PO_4 at 180 °C caused electrochemically active surface area loss, reduced ORR activity and supported Pt crystallite growth, Co/Ni dissolution, and surface reorganisation. Comparatively, reduced graphene oxide-supported catalyst was more resistant to ripening and dealloying than its Ketjen black analogue, and Pt–Ni alloy was more stable than Pt–Co. Overall, the results disentangle the roles of the carbon support and alloy composition and outline activity – stability trade-offs that guide the design of low-Pt loading cathodes for HT-PEMFCs.

Received 19th September 2025,
Accepted 24th December 2025

DOI: 10.1039/d5ey00279f

rsc.li/eescatalysis

Broader context

The transition to a low-carbon energy economy increasingly relies on hydrogen as an energy carrier for storage, decarbonization of existing technologies, or transportation applications. Among hydrogen conversion technologies, fuel cells attract significant attention of study. High-temperature proton exchange membrane fuel cells (HT-PEMFCs) offer distinct advantages over their low-temperature counterparts, including efficient recovery of reaction heat, simplified cooling, and reduced hydrogen purity requirements. However, their long-term viability and commercialisation critically depend on the development of catalysts that remain durable and active under harsh operating conditions (phosphoric acid, 180 °C). Alloying Pt with transition metals in combination with suitable carbon supports provides a strategy to lower Pt loading while maximising efficiency and durability. In this study, three alloy catalysts – Pt–Co on Ketjenblack carbon, Pt–Co on reduced graphene oxide, and Pt–Ni on Ketjenblack carbon – are evaluated against a commercial Pt/C catalyst. The comparison focuses on changes in composition, morphology, and oxygen reduction reaction activity after exposure to hot phosphoric acid, aiming to identify optimal alloy/support combinations for stable HT-PEMFC performance.

[a] Department of Inorganic Technology, University of Chemistry and Technology Prague, Technická 5, 166 28 Praha, Czech Republic. E-mail: bystront@vscht.cz
[b] Department of Organic Technology, University of Chemistry and Technology Prague, Technická 5, 166 28 Praha, Czech Republic
[c] Electrochemical Process Engineering, University of Bayreuth, Universitätsstraße 30, Bayreuth 95447, Germany
[d] Department of Materials Chemistry, National Institute of Chemistry, Hajdrihova 19, p.p. 660, SI-1001 Ljubljana, Slovenija
[e] ReCatalyst, Hajdrihova 19, 1001 Ljubljana, Slovenia

1 Introduction

The utilisation of H_2 as an energy carrier is poised to play a pivotal role in the global transition from fossil fuels to renewable energy sources.[1] In this emerging energy paradigm, H_2 will be produced through the electrolysis of water using electricity generated from renewable sources, which subsequently has the

potential for numerous applications in the chemical industry and for managing fluctuations in the electricity grid.[2] A direct conversion of H_2 chemical energy into electricity, bypassing the need for a transformation step between thermal and mechanical energy in internal combustion engines, is made feasible through fuel cells.[3] Several types of fuel cells are known, but for small to medium stationary or mobile applications,[4] at present a low-temperature (LT) and particularly high-temperature (HT) proton-exchange membrane fuel cells (PEMFC) appear to be the most promising systems.

Low-temperature PEMFCs operate with a proton-exchange membrane, typically based on a perfluorinated sulfonated polymer (*e.g.*, Nafion®), serving as a polymer electrolyte. Most LT-PEMFCs utilise H_2 and O_2, resulting in the production of water. The key advantages of LT-PEMFCs are their high energy efficiency and power density per unit weight (this applies to the FC itself, and not the heat exchange unit, see below). The relatively low operating temperature of LT-PEMFCs, around 70 °C, offers the benefit of reasonable stability of materials during prolonged operation (slow degradation of materials) and enables quick starts, including the possibility of cold starts.[5]

However, the low operating temperature of LT-PEMFCs does present severe practical challenges. These cells are extremely sensitive to impurities like CO, which act as catalyst poisons.[6] Moreover, effective water management is essential because the perfluorinated sulfonated polymer membranes require sufficient humidity for proper operation. On the other hand, too much humidity in the system leads to catalyst layer flooding which causes severe mass transport limitations. Most importantly, the heat exchange unit of LT-PEMFC requires a significant heat exchange surface making it heavy and bulky. Finally, the waste heat generated by LT-PEMFCs remains underutilised.[7]

These disadvantages can be effectively addressed by HT-PEMFCs, which operate at temperatures ranging from 160 to 180 °C. At these temperatures, perfluorinated sulfonated polymers dry out and lose their ionic conductivity. Instead, polybenzimidazole (PBI)-based membranes doped with concentrated H_3PO_4 are usually used.[8–14] HT-PEMFCs are not sensitive to the presence of CO at concentrations of up to 3 vol%, allowing for the use of H_2 derived from sources like CH_3OH, natural gas, or propane.[5] HT-PEMFCs also do not require complicated water management, as the water produced exits the cell in gaseous form. The higher operating temperature permits the use of a more compact and lighter cooling system, facilitates temperature control, and enables the utilisation of waste heat, *e.g.*, for steam cogeneration.[15,16] Nevertheless, the presence of H_3PO_4 leaching from the membrane induces corrosion of other cell components, and H_3PO_4 (including its impurities) can block the catalyst surface, leading to mediocre cell performance during operation.[17–21]

In the case of PEMFCs, electrochemical reactions occur within the catalytic layers of anodes and cathodes, which are supplied with H_2 and air/O_2, respectively, and are in contact with the proton-exchange membrane. It is widely accepted that selection of especially the cathode electrocatalyst catalysing the O_2 reduction reaction (ORR) remains the most challenging task. First, sluggish ORR kinetics usually leads to a high activation overpotential and significant energy efficiency losses.[22–24] Secondly, the low stability of cathode catalysts represents an additional issue.[25,26] Currently, Pt nanoparticles immobilised on a carbon support represent the state-of-the-art ORR electrocatalyst in an acidic environment.[27,28] Interestingly, various Pt alloys with Co, Ni, or Cu show potential to enhance the electrocatalytic activity towards ORR in aqueous environments.[29–38] The presence of an alloying metal modifies the catalyst surface, potentially increasing its intrinsic catalytic activity. Therefore, a partial replacement of Pt with less rare metals could lead to a significant reduction of catalyst cost.[39,40]

The electrochemical behaviour of an alloy catalyst significantly depends on its composition and morphology. It is important to note that its structure and composition may evolve during PEMFC operation. This phenomenon is not yet fully understood and is currently extensively investigated.[21,41–43] The influence of H_3PO_4 itself and its impurities (*e.g.* H_3PO_3) on the cell performance is substantial.[18,41,44–48] It is also widely accepted that during the operation of Pt–Co(Ni) alloy catalysts in an acidic environment, Co(Ni) dissolves from the surface, thereby exposing the electrochemically active sites of the Pt catalyst.[49–51] This process, occurring due to the limited stability of alloy catalysts, is known as (electro)chemical dealloying and/or leaching and represents one of the inevitable phenomena associated with their use.[52] While initial catalyst activity is enhanced by this process, further degradation usually leads to a significant decrease in specific activity of catalysts.[41–43] The amount of Co(Ni) in the alloy, as well as the conditions under which (electro)chemical dealloying occurs (electrode polarisation, temperature, impurities present in the H_3PO_4, *etc.*), affect significantly the catalyst's electrochemical behaviour. This is manifested by changes, *e.g.*, in surface morphology, the distribution of metal nanoparticle sizes or porosity of the support.[50]

Catalyst activity is also influenced by the type of its support. Carbon-black-based materials currently represent the standard materials. Other studied materials with potential for application are graphene derivatives such as reduced graphene oxide (rGO), which possess distinct physicochemical properties compared to carbon black. They exhibit superior electronic conductivity, higher 2D crystallinity, and fewer structural defects due to the higher carbon content in sp^2 hybridisation.[53] Some observations suggest that these properties might result in improved thermodynamic stability and, consequently, potentially prolonged catalyst lifetime during fuel cell operation.[54,55]

The present work deals with alloy catalysts synthetises by a novel method, namely Pt–Co on amorphous Ketjen black (KB) carbon support (Pt–Co/KB), Pt–Co on reduced graphene oxide (rGO) support (Pt–Co/rGO) and Pt–Ni on KB support (Pt–Ni/KB).[56] The catalysts are compared with a commercial Pt catalyst on carbon black support (Pt/C). The aim of this work is to determine the ORR activity of the studied catalysts in aqueous and H_3PO_4 media at ambient and elevated temperature, respectively. For a deeper understanding, the changes of the ORR activity of the catalysts during interaction with H_3PO_4

at elevated temperature and the composition and structural changes of the catalysts after interaction with concentrated H_3PO_4 at elevated temperature, were analysed.

2 Experimental

2.1 Used chemicals and materials

Chemicals used in this work were: 85 wt% H_3PO_4 (extra pure, Acros Organics), crystalline H_3PO_4 (>99.999% trace metal basis, Merck), 30 wt% H_2O_2 (per analysis, nonstabilised, Lach-Ner), *N*,*N*-dimethylformamide (per analysis, Penta), 10 wt% solution of polybenzimidazole in *N*,*N*-dimethylformamide (PBI Performance products), Liquion® 1100 (5 wt% propan-2-ol solution of Nafion®, IonPower), 40% Pt on carbon black (Vulcan XC-72) HiSPEC4000 (Johnson Matthey, UK), 35 wt% HCl (per analysis, Penta), 65 wt% HNO_3 (per analysis, Penta), 70 wt% $HClO_4$ (per analysis or Supra-Qualität, Roth ROTIPURAN®), propan-2-ol (per analysis, Penta), acetone (per analysis, Penta), O_2 (99.5%, SIAD), N_2 (99.99%, SIAD) and CO (99.5%, Linde). Demineralised water used during the work was prepared by DIWA 3rica system (WATEK, Czechia), conductivity <1 μS cm^{-1}, or Milli-Q® (Direct-16, Merck, Germany), conductivity <5 μS cm^{-1}. Investigated alloy catalysts Pt–Co/KB, Pt–Ni/KB and Pt–Co/rGO were prepared according to procedure specified in Sections S1.1 and S1.2 in SI. Catalysts were provided by the National Institute of Chemistry (Pt–Co/rGO) and ReCatalyst (Pt–Co/KB and Pt–Ni/KB). All weighing in the work was performed on analytical balances (MS304TS, Mettler-Toledo).

H_2O_2 was used for purification and concentration of H_3PO_4.[44,57] The 85 wt% H_3PO_4 was mixed with the 30 wt% H_2O_2 in volumetric ratio of 2 : 1. The mixture was poured in a PTFE beaker, slowly heated to 160 °C and left at this temperature for 24 h. Thus prepared concentrated H_3PO_4 was poured in a glass storage bottle while still hot and its concentration was determined by acid–base titration using automatic titrator (Easy Pro, Mettler Toledo). 0.1 M NaOH (Standard solution, Penta) was used as a titration agent. The concentration of H_3PO_4 was 97.6 ± 0.6 wt% (*i.e.*, 70.9 wt% P_4O_{10}) with volumetric density of 1.849 ± 0.006 g cm^{-3} corresponding to the expected literature value.[58,59] This H_3PO_4 was used for all measurements.

2.2 Set-up for ORR activity of the catalysts in $HClO_4$ at 25 °C

2.2.1 ORRs kinetic parameters evaluation of pristine catalysts. The working electrode was a glassy carbon rotating disk electrode (RDE, 5 mm diameter) with PTFE insulation (Pine Research, USA). Before each ink deposition, the electrode was polished with a sandpaper (MicroCut P4000, Buehler, USA) and then with a suspension of alumina (0.3 μm) on felt. Thin film electrodes were prepared from the catalysts according to the following procedure: 80 cm^3 of demineralised water, 20 cm^3 of 2-propanol and 1 cm^3 of Nafion stock solution were mixed. After that, 10 cm^3 of this solution was mixed with catalyst to achieve an overall metal concentration of 0.2 g dm^{-3}. The suspension was treated in ultrasonic bath (Bandelin, PT102H, Germany) for 15 min. Afterwards the suspension was vigorously shaken (10 s) and left to rest for 10 minutes before proceeding with further ultrasonication (15 min). The process was repeated (3–5 times) until stable ink was obtained. Then, one 10 mm^3 drop was placed onto the RDE disk using the micropipette (Fischer Scientific, USA) in order to obtain catalyst loading corresponding to 10 μg_{metals} cm^{-2}. To prevent the catalyst agglomeration in the catalytic ink during deposition, it was stirred vigorously with a PTFE magnetic stirrer (1 cm length) at 500 rpm (MR3004, Heidolph, Germany). Thin film-modified electrodes were then allowed to dry and stored in a dry box under N_2.

Measurements were performed in a glass electrochemical cell (50 cm^3). The electrolyte was aqueous solution of $HClO_4$, the cell was maintained at 25 °C using a thermostat (PC14 DC 10, Haake, Germany). To enable broader comparison with literature data and ensure robust validation of the measured values, experiments were conducted at two $HClO_4$, concentrations: 0.5 mol dm^{-3} and 0.1 mol dm^{-3}. The results were consistent across both conditions; therefore, subsequent measurements were performed exclusively in 0.1 mol dm^{-3} $HClO_4$. Measurements were performed on a potentiostat (PGSTAT302N, Autolab Metrohm, Switzerland), RDE revolution was controlled by a rotor (AFMSRCE, Pine Research, USA). Athree-electrode setup was used. The counter electrode was a Pt wire of about 260 mm^2 placed in a glass tube separated from the main compartment of the electrolyte by a porous frit. The reference electrode was a fresh reversible hydrogen electrode (RHE, Hydroflex, Gaskatel GmbH, Germany), placed directly into the electrolyte solution. The working electrode was carried in a shaft (Pine Research, USA) and placed approximately 5 mm below the electrolyte level.

Each prepared thin film electrode was first stabilised by potential cycling (200 cycles between 1.2 and 0.05 V *vs.* RHE, sweep rate of 300 mV s^{-1}) in the N_2 saturated electrolyte before the LSV measurement. Subsequently, the LSVs on the prepared thin film electrodes were measured in the potential range (1.0 V to 0.05 V *vs.* RHE) at electrode revolution rates of 400, 900, 1600 and 2500 rpm and at a sweep rate of 10 mV s^{-1} in the N_2 saturated electrolyte and then in O_2 saturated electrolyte. The currents measured in the N_2 saturated electrolyte were subtracted from the currents obtained in the O_2 saturated electrolyte. To evaluate the electrochemically active surface area (ECSA), the electrolyte was, immediately after measuring the ORR (*i.e.*, in the same experimental setup), for 60 s saturated with CO, and then 10 min purged with N_2. This was followed by 2 cycles of CV (0.05 V to 1.0 V *vs.* RHE) at a sweep rate of 20 mV s^{-1} on stationary electrode. A numerical integration (trapezoidal method) was used to integrate the CO-stripping region. A value of 450 μC cm^{-2} was used as the specific charge for the electrochemical desorption of the CO monolayer. All experimental voltammograms were corrected for the *IR* drop during the measurement. The value of 1.170 V is used as $E^{\circ}_{ORR,T}$ in 0.1 M $HClO_4$, 25 °C, O_2 saturation, O_2 activity was corrected using H_2O vapour pressure over the solution, see ref. 60. The current densities were in all cases determined with respect to

the geometric surface area of the electrode. The Koutecky–Levich (K–L) analysis (eqn (1)) of voltammograms measured at various revolution rates provided the kinetic current density values (j_k), which were subsequently used to evaluate the Tafel slope.

$$\frac{1}{j} = \frac{1}{j_{lim}} + \frac{1}{j_k} \quad (1)$$

The limiting current density j_{lim} is taken as the median of the points lying within a 20 mV interval in the region of most negative current densities j. To ensure reproducible results, each measurement was performed in triplicate and with at least three different working electrodes. A representative set of voltammograms measured at RDE (revolution rate of 1600 rpm, 20 mV s^{-1}, in 0.1 M $HClO_4$) is shown in Fig. S2.1, see SI. In addition to that, K–L analysis using voltammograms measured at various revolution rates of (400–2500 rpm, sweep 10 mV s^{-1}, in 0.5 M $HClO_4$) was performed, see resulting Tafel plots shown in Fig. S2.2 in SI. Both methods (analysis of j_k obtained from LSV at 1600 rpm and j_k obtained from LSVs at multiple revolution rates) provided comparable parameters.

2.2.2 ORRs kinetic parameters evaluation of catalysts after degradation in conc. H_3PO_4 at 180 °C. The working electrode was a glassy carbon (GC) rod (Sigradur G®, HTW, Germany) of 5 mm diameter. Before each ink deposition, the electrode was polished with sandpaper (MicroCut P4000, Buehler, USA) and then with a suspension of alumina (0.05 μm, MasterPrep®, Buehler, USA) on felt. To prevent the ink loss from the GC rod disk during catalyst application, its sides were wrapped with several layers of PTFE tape. The thin film rotating rod disk electrodes (RREs) were prepared according to the following procedure: catalyst was dispersed in 2 cm^3 of water to achieve an overall metal concentration of 1 mg cm^{-3}. The suspension was treated in ultrasonic bath (ASonic, PRO 100, China) for 15 min. Afterwards the vial was vigorously shaken (10 s) and left to rest for 10 min before proceeding with further ultrasonication (15 min). The process was repeated until stable ink was obtained. Then, one 20 mm^3 drop was applied to the GC rod base (disk) using a micropipette (Eppendorf, Germany) in order to obtain catalyst loading corresponding to 10 μg_{metals} cm^{-2}. The surface of the disk was allowed to dry at room temperature and then drop (*ca.* 7 mm^3) of Nafion stock solution (diluted 1 : 50 with propan-2-ol) was placed onto the rod disk. Subsequently, 20 mm^3 of purified 97.6 wt% H_3PO_4 (diluted 1 : 9 with water) was dropped onto the thin film and the rods were placed in an oven (SP-55 Easy, Kambič, Slovenia) pre-heated to 180 °C for catalyst degradation. After defined heating time (1, 3, 8, 24 and 72 h), the rods were gradually removed from the oven and used for electrochemical tests.

Electrochemical characterisation of thin film-modified RREs was performed in a glass electrochemical cell (50 cm^3). The electrolyte was 0.1 mol dm^{-3} $HClO_4$, the cell was maintained at 25 °C using a thermostat (PC14 DC 10, Haake, Germany). Measurements were performed on a potentiostat (CompactStat.e, IVIUM Technologies, Netherland), electrode revolution rate was controlled by an electrode rotator (AFMSRCE, Pine Research, USA). A three-electrode setup was used. The counter electrode was a graphite rod (SPK grade, Ultra "F" purity, Thermo Scientific, USA) of about 40 cm^2 placed in a glass tube separated from the main compartment of the electrolyte (through a thin connection tube). The reference electrode was a fresh RHE (Hydroflex, Gaskatel GmbH, Germany), placed separately and connected with the measuring cell by a glass bridge filled with the same electrolyte. The working RRE was mounted into an in-house made shaft and its tip was immersed approximately 5 mm below the electrolyte level. The shaft was constructed from CNC axis with centering and adjusted to a precise diameter on a lathe.

After degradation, each prepared thin film-modified RRE was first cycled 50 times in the potential range of 1.0 to 0.05 V *vs.* RHE at a sweep rate of 300 mV s^{-1} in the N_2 saturated electrolyte. Subsequently, the LSVs of the prepared thin film-modified RREs were measured in the potential range (1.0 V to 0.05 V *vs.* RHE) at a sweep rate of 20 mV s^{-1} in the O_2 saturated electrolyte at revolving electrode (1600 rpm). To evaluate the ECSA immediately after measuring the ORR (*i.e.*, in the same experimental setup), the same protocol as described in Section 2.2.1 was used. All experimental voltammograms were corrected for the *IR* drop. The value of 1.170 V is used as $E^{\circ}_{ORR,T}$ (25 °C, O_2 saturation, pH value of 0.1 M $HClO_4$, O_2 activity was corrected using H_2O vapour pressure over the solution, see ref. 60). The current densities were in all cases determined with respect to the geometric surface area of the electrode. The Koutecky–Levich (K–L) analysis (eqn (1)) of voltammograms measured at various revolution rates provided the kinetic current density values (j_k), which were subsequently used to evaluate the Tafel slope. The limiting current density j_{lim} is taken as the median of the points lying within a 20 mV interval in the region of minimum current densities j. To ensure reproducible results, each measurement was performed in triplicate and with at least three different working electrodes.

2.3 Leaching of the catalyst powders in conc. H_3PO_4 at 180 °C

2.3.1 Experimental setup. To determine stability of the catalysts, 30 mg of catalyst sample was mixed with 350 mm^3 of 97.6 wt% H_3PO_4 in a glass vial with PTFE cap. This mass ratio of catalyst to H_3PO_4 is similar to the mass ratio of these components in a real HT-PEMFC. The vials were placed in an aluminium block positioned on a laboratory heater (MR3004, Heidolph, Germany) and heated to 180 °C. Various catalyst samples were leached for 1, 3, 8, 24 or 72 h. After this leaching, the suspension was washed (10 × 1 cm^3) with demineralised H_2O and the liquid fractions were collected after centrifugation (MiniSpin Eppendorf, Germany) at 13 700 rpm. The combined liquid fractions were diluted to a total volume of 20 cm^3. The solid fraction was then decanted several times with demineralised water until neutral pH of the suspension was achieved and then dried under N_2 at room temperature. The solid residue was split in two parts. The first part was analysed by the various instrumental methods (XRD, XRF, XAS, Raman spectroscopy, XPS and TEM), the second one (about 15 mg) was dissolved in aqua regia (4 cm^3 conc. HNO_3 + 12 cm^3 conc.

HCl, 24 h, boiling under reflux). The aqua regia solution was then diluted to 200 cm^3 and (after decantation of undissolved carbon) analysed by IPC-OES. Triplicate measurements were taken only at time 0 h and 24 h, the other times are represented by only one sample.

2.3.2 Analysis of liquid fractions; ICP-OES. The leachates were analysed for the presence of Co, Pt, and Ni ions by ICP-OES (Optima 8000, PerkinElmer, USA). The calibration was performed at following wavelengths: 228.616 nm and 238.892 nm for Co, 214.423 nm, 265.945 nm for Pt and 221.648 nm, 231.604 nm for Ni. Each calibration series included 8 standards in the concentration range of 0.1–100 mg dm^{-3}.

2.3.3 Analysis of the solid samples; XRD, XRF, XPS, Raman spectroscopy, TEM-EDS, XAS. XRD measurements were performed on a PANanalytical X'Pert PRO diffractometer (PANanalytical, Holland) with Co lamp ($K\alpha_1$, wavelength 1.7903 Å), step size of 0.0390° 2θ, data were evaluated with PDF-4+ (2018) – Powder Diffraction File (ICDD- International Centre for Diffraction Data).

For XRF measurements performed with a Performix spectrometer (Thermo ARL, Switzerland) with Rh lamp (4.2 kW), the samples were deposited on Ge (111) crystal. Standard-free analysis using the UNIQUANT software integrated into software Oxsas was used for processing the obtained data.

Raman spectra were measured with a dispersive Raman spectrometer model DXR Raman Microscope (Thermo Scientific, USA) equipped with an Olympus confocal microscope. The excitation source was a diode-excited Nd:YAG laser with a wavelength of 532 nm and an input power of 10 mW. A lattice of 900 notches mm^{-1} was used. A multichannel thermoelectrically cooled CCD camera was used as detector. The samples were measured with a 50× objective with a measurement footprint of about 1 μm^2. The samples were measured through a 50 μm slit aperture. Measurements were performed with a power of 0.3 mW, measurement time of 30 s and 10 spectral accumulations, with photobleaching for 30 s. Three spots from each sample were measured.

XPS measurements were performed on an Omicron ESCA Probe P (Scienta Omicron, Germany). Survey spectra were measured with 0.4 eV step and pass energy 50 meV. Excitation source was Al with energy Kα = 1486.7 eV, pressure in chamber around 3.5×10^{-10} mbar.

EFTEM Jeol 2200 FS (Jeol GmbH, Germany), 200 kV EFTEM with Schottky FEG and In-Column Omega Energy-filter was used for TEM analysis of samples of the leached catalysts. Energy dispersive spectroscopy (EDS, Oxford Instruments, UK) with a resolution of 1–2.4 nm was used for elemental analysis.

The *ex situ* XAS measurements were performed at the P64 beamline (DESY, Hamburg, Germany). Samples of the pristine catalysts and catalysts after leaching were deposited between two Kapton tapes (80 μm, DuPont, USA) to achieve loading of approximately 1 mg_{metals} cm^{-2}. The measurements were performed in fluorescence (PIPS detector) and transmission mode. Although both detection modes yielded comparable results, fluorescence measurements provided a better signal-to-noise ratio. However, self-absorbance effects were assessed by comparison with transmission data and corrected when necessary. Spectra at the Pt L_3-edge and Co and Ni K-edges were collected. The corresponding metallic foils were measured simultaneously with the samples to align the energy. The software Bessy_47b and SimXLite, both developed by the beam scientists at KMC-3 beamline (BESSY II – Berlin), were used for the data processing and EXAFS fitting, respectively. The ranges used for the EXAFS fit were k = (2.0; 12.0) $Å^{-1}$ and R = (1.0; 3.0) Å for Pt L_3-edge, and k = (4.0; 12.0) $Å^{-1}$ and R = (1.0; 3.0) Å for Co K-edge, and k = (3.0; 11.0) $Å^{-1}$ and R = (1.0; 3.0) Å for Ni K-edge. The metallic foils were used to determine the amplitude factor, S_0^2, that was equal to 0.867, 0.796 and 0.787 for Pt L_3-edge, Co K-edge and Ni K-edge, respectively. The scattering paths were obtained using the FEFF8 software.

The *in situ* XAS measurements were performed at the P65 beamline (DESY, Hamburg, Germany). Pristine catalyst was dispersed in 15 cm^3 of *N*,*N*-dimethylformamide to achieve an overall catalyst concentration of 14 mg cm^{-3}. Subsequently, a PBI solution in DMF was added to reach a catalyst-to-PBI mass ratio of 1 : 0.11. The resulting suspension was homogenised in an ice bath using an ultrasonic probe (Sonoplus MS73, Bandelin, Germany) operated at 12 W for 30 minutes. The ink was then deposited onto a square piece of gas diffusion layer (6 cm × 6 cm, GDL, Sigracet 38BC®, SGL, Germany) using a computer-controlled ultrasonic spray coater (CNC platform by CZRobotics, ultrasonic spray system by Cheersonic) equipped with a 0.5 mm ultrasonic tip (6 W, N_2 flow 50 cm^3 min^{-1}). The GDL was placed on a hot plate preheated to 110 °C. The ink, stored in a 10 cm^3 syringe, was fed to the ultrasonic spray tip *via* a hose using an automatic syringe pump (NE-1000, KFTechnology, Italy) at a flow rate of 0.5 cm^3 min^{-1}. Following deposition, the hot plate temperature was raised to 190 °C for 30 minutes to complete the drying process. The coated GDE was then allowed to cool on the plate and stored in a dry box under N_2 atmosphere. The final catalyst loading (1 mg_{metals} cm^{-2}) was verified by comparing the mass of the coated GDE to that of the pristine GDL.

For monitoring *in situ* degradation *via* XAS, a custom-designed in-house cell allowing spectra recording during cell heating was employed. Detailed cell description and photographs of the complete cell assembly are provided in the Section S1.3 and Fig. S1.1 in SI. This setup was chosen for its similarity to the H_3PO_4 leaching setup used in this study (*i.e.*, simple leaching without polarisation). In future research, it would be advisable to use an *in situ* setup allowing electrode polarisation (for example, during the ORR process) while maintaining a temperature of 180 °C and an environment of concentrated H_3PO_4 (in-*operando* regime).

2.4 Set-up for ORR activity of the catalysts in conc. H_3PO_4 at elevated temperature

2.4.1 ORRs kinetic parameters evaluation. The working electrode was a 5 mm diameter glassy carbon rod Sigradur G® (HTW, Germany). Before each ink deposition, the electrode was polished with sandpaper (MicroCut P4000, Buehler, USA) and then with a suspension of alumina (0.3 μm) on felt. To prevent the ink loss from the RRE disk during catalyst

application, its sides were wrapped with several layers of PTFE tape (the PTFE tape was removed after final drying). The thin film electrodes were prepared according to the following procedure: catalyst was dispersed in 10 cm^3 of acetone to achieve an overall metal concentration of 0.2 g dm^{-3}. The mixture was homogenised in an ice bath using an ultrasonic probe (Sonoplus MS73, Bandelin, Germany) for 30 minutes, power 12 W. To achieve final metal loading of 10 μg_{metals} cm^{-2}, a total of 10 mm^3 of ink was applied dropwise (2 mm^3 per drop) to the GC rod base using a micropipette (Eppendorf, Germany). After each drop, the surface of the disk was allowed to dry at room temperature. During thin film preparation, the catalytic ink was vigorously stirred with a PTFE magnetic stirrer (1 cm length) at 500 rpm using hotplate (MR3004, Heidolph, Germany) to prevent catalyst agglomeration. Then, for immobilisation of the thin film on the surface of the electrode, 4 mm^3 of PBI solution in dimethylformamide (0.5 g_{PBI} dm^{-3}) were applied in two drops on the surface of the thin film. The PBI solution was vigorously stirred at 500 rpm for at least 1 h before and during deposition. The prepared RREs were dried at ambient temperature and stored in a dry box under N_2.

The measurements were carried out in a PTFE vessel (100 cm^3) placed in a heating mantle (WiseTherm WHM, Witeg) heated to 120, 140, 160 or 180 °C using purified 97.6 wt% H_3PO_4 as an electrolyte solution. All measurements were performed using a potentiostat EC301 (Stanford Research Systems, UK). A rotator with rotation control (AFMSRXE, Pine Research, USA) was used in combination with an in-house made shaft. The shaft was constructed from CNC axis with centering and adjusted to a precise diameter on a lathe. The temperature of electrolyte was monitored by a thermocouple (5SRTC, Omega, USA) placed in a glass tube and controlled automatically by an in-house made temperature controller. The counter electrode was a roll of Pt foil with an area of about 7 cm^2 separated from the main compartment of the electrolyte by a ceramic frit. MSE ($Hg|Hg_2SO_4$ in $K_2SO_{4sat.}$ solution, Monokrystaly, Czechia) was used as the reference electrode. It was separated from the hot H_3PO_4 environment by a double junction, the first one filled with 97.6 wt% H_3PO_4, the second with saturated K_2SO_4 solution. The second junction was placed in a short Liebig cooler tempered to 25 °C by a cryostat (Julabo F12). The cell was sealed with PTFE tape (DuPont, USA).

Each prepared thin film-modified electrode was first cycled 3 times in the potential range from 0.3 V to −0.1 *vs.* MSE (sweep rate 100 mV s^{-1}) in the N_2 saturated electrolyte. Subsequently, the LSVs were measured in the same potential range at a sweep rate of 5 mV s^{-1} in the N_2 saturated electrolyte (minimum saturation time 15 min) and then in O_2 saturated electrolyte (minimum saturation time 15 min) at revolving RRE electrodes (400, 900, 1600 and 2500 rpm). Currents measured in N_2 saturated electrolyte were subtracted from the currents obtained in the O_2 saturated electrolyte. All measurements were performed at various temperatures (120 °C then 140 °C, 160 °C and finally 180 °C, whole series typically takes from 3 to 5 hours).

The potentials measured using MSE reference electrode (at each temperature) were recalculated to RHE scale. For this purpose, an in-house made RHE (Pt wire coated with Pt black immersed directly in H_2 saturated H_3PO_4 electrolyte) was used in the same setup, without the use of additional electrodes or gas saturation. Potentials between MSE and RHE were measured over the temperature range of 120–180 °C. This dependence can be approximated by the equation in eqn (2) (R^2 = 0.975 for the temperature range of 120–180 °C).

$$E_{MSE,t} = -694.6\ mV + t{\cdot}0.70\ mV\ {}^{\circ}C^{-1} \quad (2)$$

where t is temperature in °C. Equilibrium potentials $E_{ORR,g,T}$ for ORR in 97.6 wt% H_3PO_4 at temperatures of 120, 140, 160 and 180 °C, for gaseous H_2O as a product, with consideration of changes in the activities of the species involved are 1.056, 1.031, 1.005 and 0.978 V, respectively. The current densities were in all cases determined with respect to the geometric surface area of the electrode. The K–L analysis (eqn (1)) of voltammograms measured at various revolution rates provided the kinetic current density values (j_k), which were subsequently used to obtain the Tafel slope. The limiting current density j_{lim} is taken as the median of the points lying within a 20 mV interval in the region of minimum current densities j. All voltammograms were corrected for the *IR* drop. The Savitzky–Golay filter (cubic, frame length 9 points) was used to process the measured data. To ensure reproducible results, each measurement was performed in triplicate and with at least three different working electrodes.

3 Results

3.1 ORR activity of the catalysts in aqueous $HClO_4$ at 25 °C

In the present work, the catalysts (composition provided in Table 1) are studied mainly in the context of their ORR catalytic

Table 1 ICP-OES, metal loss due to leaching in 97.6 wt% H_3PO_4 at 180 °C for 24 h, in liquid fraction expressed as wt% loss of leached metal (with respect to the pristine mass), in leached samples by total dissolution in aqua regia

			After 24 h leaching			
	Pristine (wt%)		In liquid fraction (wt%)		Remaining in alloy (wt%)	
Catalyst type	Pt	Co(Ni)	Pt	Co(Ni)	Pt	Co(Ni)
Pt/C	38.1 ± 0.9	—	0.1 ± 0.1	—	31.4 ± 0.7	—
Pt–Co/KB	25.3 ± 0.4	1.9 ± 0.1	3.3 ± 0.2	1.8 ± 0.1	11.7 ± 0.1	0.0 ± 0.2
Pt–Co/rGO	31.0 ± 0.1	3.9 ± 0.1	0.5 ± 0.1	1.0 ± 0.1	25.4 ± 0.1	1.3 ± 0.1
Pt–Ni/KB	28.2 ± 1.3	7.1 ± 0.6	1.7 ± 0.2	3.2 ± 0.9	19.7 ± 2.5	3.8 ± 0.2

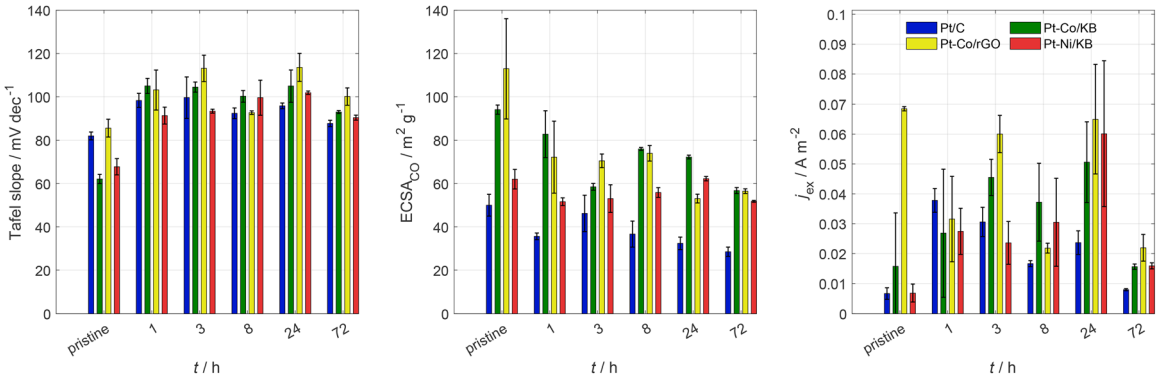

Fig. 1 ORR kinetic parameters of H_3PO_4–leached catalysts determined in 0.1 mol dm^{-3} $HClO_4$ at 25 °C. LSV, 1600 rpm, 20 mV s^{-1}, corrected for background currents and uncompensated resistance, use of corresponding $E_{ORR,i,T}$, thin film on GC RRE (10 μg_{metals} cm^{-2} of catalyst after leaching in 97.6 wt% H_3PO_4 at 180 °C for 0–72 h).

activity for HT-PEMFC application, *i.e.* in concentrated H_3PO_4 at elevated temperatures. However, to get an overview of the application potential of these catalysts, their activity towards ORR was also investigated in aqueous $HClO_4$ solution at room temperature. The obtained Tafel slope, ECSA and j_{ex} values are summarised in Fig. 1 (marked as "pristine") and in Table S2.1 in SI.

Pt–Co/C and Pt–Ni/C catalysts exhibit lower values of Tafel slope (Fig. S2.1 in SI) than the used benchmark material Pt/C. On the other hand, the Tafel slope of Pt–Co/rGO is slightly higher than the benchmark. All experimental alloy catalysts also possess a higher ESCA value. In particular, the ECSA in case of Pt–Co/rGO is more than double compared to Pt/C. All alloy catalysts also achieve higher j at negative overpotentials observed in the LSV curve (Fig. 2) compared to Pt/C. For example, at 0.9 V *vs.* RHE, the values are as follows: Pt/C: j = −13.5 A m^{-2}, Pt–Co/KB: j = −35.7 A m^{-2}, Pt–Co/rGO: j = −20.0 A m^{-2}, and Pt–Ni/KB: j = −34.5 A m^{-2}.

Subsequently, the same parameters were evaluated for the catalysts after 1–72 h of exposure to concentrated H_3PO_4 at 180 °C (leaching) by RRE. Determined parameters are summarised in Fig. 1 and numerically in SI, Table S2.1, example of LSV curves for Pt/C are show in Fig. S2.2 in SI.

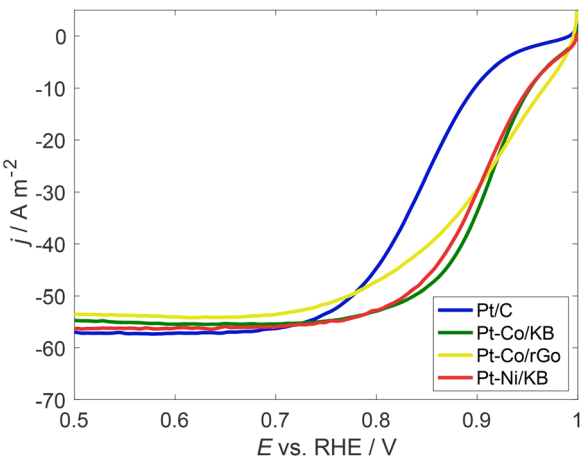

Fig. 2 LSV, 1600 rpm; RDE electrode, 25 °C, 10 μg_{metals} cm^{-2} of catalyst, 0.1 mol dm^{-3} $HClO_4$, 20 mV s^{-1}, corrected for background currents and uncompensated resistance.

The measured values show that already after the first hour of catalysts leaching in concentrated H_3PO_4 at elevated temperatures, the Tafel slope value increases for all catalysts. However, this value subsequently decreases with prolonged leaching time, and after 72 h, it reaches similar values for all catalysts (~90 mV dec^{-1} for Pt/C, Pt–Co/KB and Pt–Ni/KB, ~100 mV dec^{-1} for Pt–Co/rGO). The ECSA decreases for all studied catalysts. The decrease in ECSA may be attributed to particle growth, which leads to a reduction in the overall surface area. However, it should also be noted that some metallic particles may detach due to support corrosion; this effect was not investigated and is assumed to be negligible. Given that purified H_3PO_4 was used for catalyst leaching, and ECSA was determined after potential cycling in excess of $HClO_4$, the decrease in ECSA was also unlikely result of phosphorous and phosphate species adsorption.[18,44,45] Interestingly, the lowest ECSA loss of about 20% (after 72 h of leaching) was observed for Pt–Ni/KB. In other cases, the ECSA dropped to about 50% of the original value. After 72 h of leaching, the best performing catalyst is Pt–Ni/KB as can be seen from the following j values at 0.9 V *vs.* RHE, (Pt–Ni/KB: j = −12.5 A m^{-2} > Pt–Co/KB: j = −10.8 A m^{-2} > Pt–Co/rGO: j = −8.9 A m^{-2} > Pt/C j = −8.2 A m^{-2}). Focusing on j_{ex}, the changes during leaching vary within one order of magnitude, generally in a non-monotonic manner in all cases, although some trends can be observed. For example, in the case of Pt/C, an initial increase in j_{ex} is followed by a downward trend. Conversely, Pt–Co/KB and Pt–Ni/KB exhibit a rising trend in j_{ex} throughout the degradation period, except for the final measurement at 72 h.

3.2 Leaching of the catalyst powders in concentrated H_3PO_4 at 180 °C

During HT-PEMFC operation, the catalysts will be exposed to concentrated H_3PO_4 at elevated temperatures (160–180 °C). Therefore, the stability of the investigated catalysts in this environment was evaluated. To establish the initial metal

composition, the pristine catalysts were firstly completely dissolved in aqua regia and the leachates were analysed by ICP-OES. Secondly, the pristine catalysts were leached in 97.6 wt% H_3PO_4 at 180 °C for 1, 3, 8, 24 and 72 h. After separating the leachate from the remaining solid catalyst, both phases were analysed to monitor compositional changes of the catalysts during leaching. In particular, the composition of the solid catalysts after leaching was determined *via* ICP-OES of the solution obtained by dissolving the solid in aqua regia, XRF and TEM/EDS spot analysis. The amount of metals leached into H_3PO_4 was obtained by ICP-OES analysis. The ICP-OES results are summarised in Tables 1 and 2. It is important to point out that there is a discrepancy in the mass balance of Pt, *i.e.* the Pt content in the pristine catalyst seems to be higher than the sum of the Pt contents in the catalyst after leaching and metal leached into H_3PO_4. This can be partly attributed to losses, which may have occurred during the centrifugation, washing, and drying steps of the samples. In addition to that, H_3PO_4 or its anions may contaminate the carbon supports during leaching, resulting in an increased support mass after leaching. It remains unclear whether this is due to surface modification, adsorption[61] or even intercalation.[62] In any case, the presence of phosphorus components in catalysts after leaching was confirmed by XPS, see Fig. S3.1 in SI. Interestingly, no non-Pt metals were seen in XPS spectra of Pt–Ni and Pt–Co catalysts, Fig. S3.2 in SI. To explain this apparent discrepancy between XPS and ICP-OES (and even XRF) results, it is important to consider differences between these techniques. ICP-OES and XRF provide information about bulk composition of the catalyst, XPS on the other hand provides information about composition of the surface layer of no more than 15–20 nm thickness. Therefore, the absence of non-Pt metals in the surface layer of even pristine catalysts suggests that they were effectively leached out from the metallic nanoparticles present on the outer surface of the carbon support. This most likely occurred during catalyst activation, *i.e.* last step of the catalyst production based on acid leaching (as in our case, see Section S1.2 in SI).

Focusing on the first two columns of Table 1, the Pt content (38.1 wt%) determined in pristine Pt/C agrees well with the information provided by the manufacturer (40 wt%). In the case of alloy catalysts, the highest Pt content (31 wt%) was found in the pristine Pt–Co/rGO, the highest content of non-Pt metal (7 wt%) was present in pristine Pt–Ni/KB. Regarding the alloy composition, Pt–Co/KB exhibits a molar ratio of 4 : 1 Pt : Co, Pt–Co/rGO shows a 7 : 3 Pt : Co ratio, and in the case of Pt–Ni/KB, the molar fraction of Pt in the alloy is around 55 mol%, see Table 2. Results of catalyst leaching in 97.6 wt% H_3PO_4 for 24 h (columns 3–6 of Table 1) clearly show that while almost no Pt is dissolved from Pt/C, a significantly higher amounts of Pt were dissolved from the alloy catalysts. In particular, the loss of Pt decreased in the following order Pt–Co/KB (13 wt%) < Pt–Ni/KB (6 wt%) < Pt/rGO (2 wt%).

The non-Pt metals leached significantly more than Pt. Based on ICP-OES results, it appears that 45 wt% of Ni, 60 wt% of Co and nearly 99.5 wt% of Co was dissolved from Pt–Ni/KB, Pt–Co/rGO and Pt–Co/KB, respectively. These values were estimated from the ratio of non-Pt metal content before and after leaching. If the increased mass of the carbon support was taken into account by assuming that the Pt mass balance (the Pt mass in the pristine catalyst minus the Pt mass in the liquid fraction must equal the Pt mass remaining in the alloy after leaching), then the non-Pt metal losses are 28 wt% of Ni, 60 wt% of Co and nearly 99 wt% of Co was dissolved from Pt–Ni/KB, Pt–Co/rGO and Pt–Co/KB, respectively. Thus, the Pt–Ni alloy exhibit under studied condition higher stability than Pt–Co alloy. A significant difference between the dissolution of Co from Pt–Co alloy in the case of the two different carbon supports can be attributed to the stabilising effect of the rGO mitigating catalyst dealloying.[63]

These results were also confirmed by XRF analyses. For relative comparison, the parameter $\rho_{Pt/X}$ is introduced, defined as the ratio between the mass fraction of Pt and that of the non-platinum metal. The specific method of its determination is indicated in the subscript ($\rho_{Pt/X,ICP}$, $\rho_{Pt/X,XRF}$ or $\rho_{Pt/X,EDS}$). Results for XRF are summarised in Table 3 and in the Table S3.1 in SI. These data also indicate a stable alloy composition in the case of Pt–Ni/KB and relative stability in the case of Pt–Co/rGO compared to the exponential increase of $\rho_{Pt/M,XRF}$ in the case of Pt–Co/KB. Interestingly, a superior stability of Pt–Co/rGO catalyst during short-term operation of HT-PEMFC was recently reported.[63] Further information about the catalysts (pristine alloy catalysts and catalysts after 24 h of leaching) was obtained by TEM in combination with EDS spot analysis, see Table 3 and Fig. S3.3–S3.5 in SI. This enabled the investigation of the compositional uniformity of alloyed nanoparticles (wt% of Pt and non-Pt metal X; $\rho_{Pt/X,EDS}$) before and after leaching in 97.6 wt% H_3PO_4 environment. As can be seen, the pristine catalysts already contains particles with a quite variable composition (expressed by $\rho_{Pt/X,EDS}$). After H_3PO_4 leaching (24 h) a part of metallic particles contains only Pt, confirming the loss of a significant part of non-Pt metal from

Table 2 ICP-OES, molar composition of alloy pristine catalyst samples, total dissolution in aqua regia, recalculated from Table 1

Catalyst type	$mol\%_{alloy}$ Pt	$mol\%_{alloy}$ Co(Ni)
Pt/C	—	—
Pt–Co/KB	80.1 ± 0.9	19.9 ± 0.9
Pt–Co/rGO	70.6 ± 0.4	29.4 ± 0.4
Pt–Ni/KB	54.4 ± 1.8	45.6 ± 1.8

Table 3 Composition of the catalyst samples before and after leaching in 97.6 wt% H_3PO_4 at 180 °C for 24 h, $\rho_{Pt/X}$ is weight ratio of Pt to non-Pt metal

Catalyst type		$\rho_{Pt/X,ICP}$	$\rho_{Pt/X,XRF}$	$\rho_{Pt/X,EDS}$
Pt–Co/KB	Pristine	13.2 ± 0.7	14.5 ± 0.2	12.2 ± 7.8
	24 h leaching	∞	27.6 ± 0.6	45.3 ± 49.8
Pt–Co/rGO	Pristine	8.4 ± 0.2	8.1 ± 0.1	5.8 ± 1.2
	24 h leaching	19.0 ± 1.5	13.8 ± 0.2	12.9 ± 8.9
Pt–Ni/KB	Pristine	4.0 ± 0.4	5.3 ± 0.1	6.3 ± 3.6
	24 h leaching	5.1 ± 0.7	6.5 ± 0.1	9.0 ± 7.2

the alloy. This trend was the same for Pt–Co/KB and Pt–Ni/KB. On the other hand, in the case of Pt–Co/rGO, the differences in particle composition before and after leaching were less significant, which is again in good agreement with the already discussed improved stability of this catalyst. It is also worth noting, that leaching of all catalysts does not only lead to the change in metals content, but also to the increased heterogeneity in their distribution, *i.e.* while there are some particles with a composition similar to that of the pristine sample, more particles containing only Pt are newly present after leaching, see column of $\rho_{Pt/X,EDS}$ and its standard deviations in Table 3.

The Raman spectra (Fig. S3.6. in SI) also show the different behaviour of the KB and rGO supports. A summary of D and G band intensity ratios (I_D/I_G) in Table 4 shows that the ratio is lower for rGO than for amorphous carbon KB support, and that the ratio does not significantly change upon leaching.

Another monitored parameter was the average size of metallic crystallites, see Fig. 3 and Table S3.2 in SI, determined by analysis of XRD patterns shown in Fig. S3.7–S3.10 in SI.

In the case of the Pt–Ni/KB catalyst, the XRD pattern (Fig. 4) shows distinct reflections corresponding to a minor Pt and dominant intermetallic tetragonal PtNi phase.[64–72] The stoichiometry of PtNi is in agreement with ICP-OES measurement, see Table 2. However, the overlap of Pt and PtNi reflections does not allow accurate determination of the crystallite size. Consequently, at least TEM images were used to estimate the particle sizes in the pristine and leached Pt–Ni/KB samples. While the particle sizes determined by TEM are not directly comparable to the crystallite sizes derived from the Pt(111) XRD reflections, the analysis clearly showed that there is no significant change in the overall particle size distribution, see Fig. S3.11 in SI.

For the Pt–Co/KB and Pt–Co/rGO catalysts, the situation is different. The reflections of relevant intermetallic phases (Pt_3Co, PtCo, or even $PtCo_3$) and Pt fall within the regions of the broad XRD peaks present in the diffractograms, see Fig. S3.7. It is, therefore, not possible to unambiguously distinguish whether any and which intermetallic phases are present in the samples alongside Pt or if the Pt–Co alloys are disordered solid solutions. The latter would not be unexpected, as the acid-leached Pt–Co alloys (as in our case, see Section S1.2 in SI) often exhibit a disordered structure, with the approximately three outermost atomic layers enriched in Pt.[72,73] Considering the small particle sizes of investigated nanoparticles (around 3 nm) and given the atomic diameter of Pt (0.27 nm[74]), such Pt enrichment would correspond to more than half of the total particle volume. To facilitate comparison, the main reflection (40–50° 2θ) is interpreted as Pt(111) reflection and the corresponding crystallite sizes are shown in Fig. 3.

The results show that catalyst leaching in 97.6 wt% H_3PO_4 at 180 °C leads in the case of Pt/C, Pt–Co/KB to a pronounced increase in average crystallite size interpreted from Pt(111) reflection. On the other hand, nanoparticles in Pt–Co/rGO and Pt–Ni/KB do not seem to grow significantly. The observed growth can be attributed to Ostwald ripening at high open circuit potential (approximately 100 mV lower *vs.* estimated E_{ORR}, for suspension of catalyst with concentrated H_3PO_4 in contact with air, *i.e.* about 20% of O_2[42,43]). For the time range of 0–24 h, the most significant crystallite size growth of about 110% was observed for Pt/C. In the case of alloy catalysts, the crystallite growth was significantly lower (39% for Pt–Co/KB, and only 10% for Pt–Co/rGO). A similar behaviour has also been observed in the literature when the same catalyst was used in a single-cell setup.[63] These results show that while almost no Pt leached from Pt/C, the catalyst changed significantly. This suggests that a significant part of the nanoparticles dissolved into Pt^{2+} ions, most of which redeposited on the larger crystallites within the catalyst. The more pronounced Pt loss and lower crystallite growth in the case of alloy catalysts can be interpreted as a greater difficulty of Pt^{2+} ion redeposition on distorted Pt alloy surfaces than on a pure Pt surface.[51] Finally, the least pronounced crystallite growth and least Pt and Co dissolution in the case of Pt–Co/rGO confirms the stabilising effect of rGO support. Thus, from this point of view, the use of rGO as a support appears promising because a smaller crystallite size implies a higher ECSA for ORR. The insignificant growth of nanoparticles within Pt–Ni/KB can likely be attributed to the presence of intermetallic PtNi phase.

The coordination numbers of Pt and Co(or Ni) (labelled X) were determined from the EXAFS fit, see Fig. 5, XAS spectra in Fig. S3.12–S3.18 in SI. The notation CN_{Pt-X} refers to a coordination number where Pt is the central atom and X represents the

Table 4 Raman spectroscopy, ratio of D and G band intensities, I_D/I_G for alloy catalysts before and after leaching in 97.6 wt% H_3PO_4 at 180 °C for 24 h

Catalyst	Ratio I_D/I_G/%
Pt–Co/rGO	0.90
Pt–Co/rGO 24 h	0.91
Pt–Co/KB	1.13
Pt–Co/KB 24 h	1.08

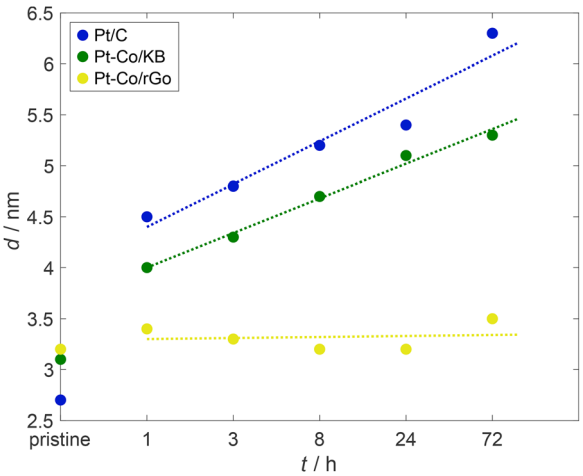

Fig. 3 Crystallite size interpreted from Pt(111) reflection of the catalyst samples before and after leaching in 97.6 wt% H_3PO_4 at 180 °C for 1, 3, 8, 24 and 72 h determined by XRD.

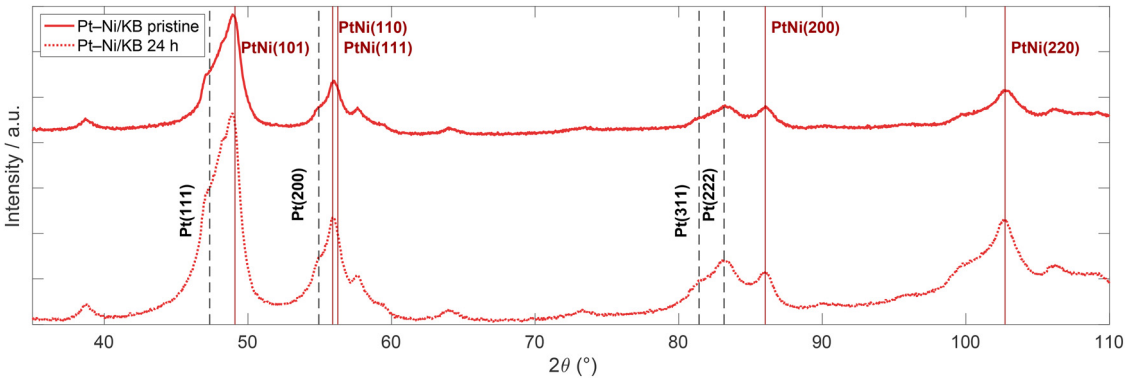

Fig. 4 XRD patterns of Pt–Ni/KB before and after leaching in 97.6 wt% H_3PO_4 at 180 °C for 24 h.

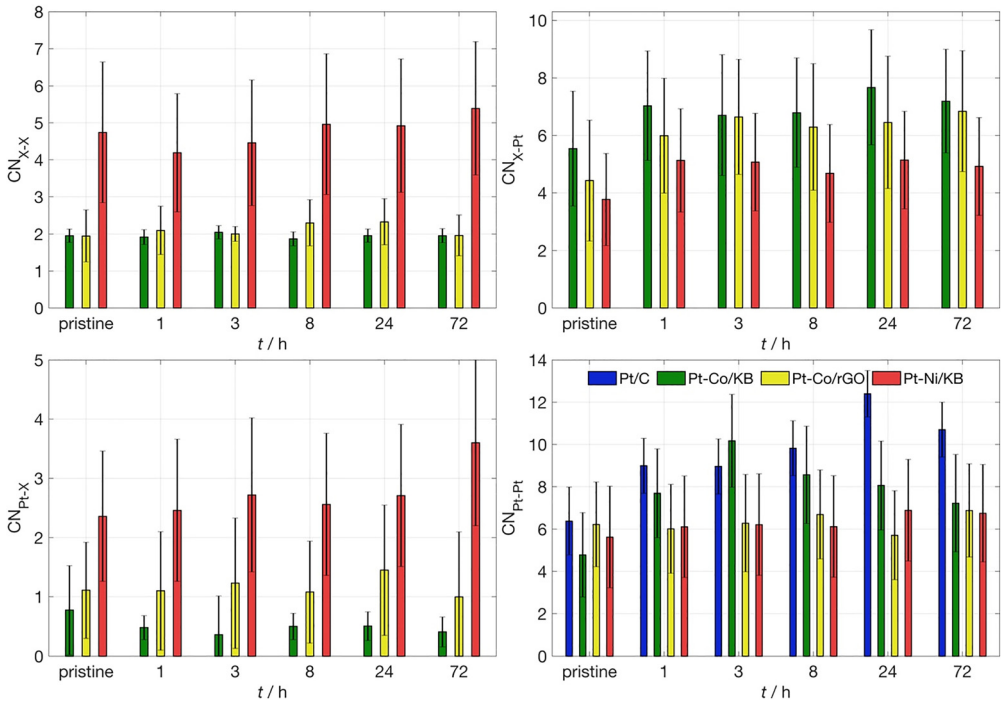

Fig. 5 EXAFS, coordination numbers, catalyst samples before and after leaching in 97.6 wt% H_3PO_4 at 180 °C for 1–72 h, X for Co or Ni, notation: Y–X – first central Y atom, second coordinating X atoms, error bars of EXAFS fit (no between replicates).

(non-Pt) coordinating atom. It can be deduced from the Pt–Pt coordination number, CN_{Pt-Pt}, increase (the ratio of surface Pt atoms to bulk atoms decreases) that the particles increase in size. Another reason for the increase in value of CN_{Pt-Pt} may be the leaching of the non-Pt metal from the alloy. Based on CN_{Pt-Pt}, the observed trend in particle size growth (Pt–Ni/KB < Pt–Co/rGO < Pt–Co/KB < Pt/C) agrees with Fig. 3. In contrast, the CN_{X-X} values are not significantly affected by the degradation. This could imply that statistically, in the nanoparticle surface layer, Ni and Co are more likely present as single atoms (which subsequently dissolve) surrounded/coordinated mainly by Pt.

On the other hand, deeper in the nanoparticles (protected from etching) the non-Pt metals are more concentrated, so that on average Co(Ni) is in direct contact with approximately 1 atom (2.5 atoms) of the same non-Pt atom. In the case of Pt–Ni/KB, the value of CN_{Ni-Ni} is relatively higher compared to Pt–Co alloys, which can be attributed to the fact that the molar concentration of Ni in the alloy is higher compared to Pt–Co alloys, see Table 2. This value can also be explained by the protecting effect that the Pt shell has on the Ni-rich core. It can be seen that, while the pristine samples have lower CN_{X-Pt} (non-Pt central atom coordinated by Pt) values, after only 1 h of leaching this value increases and than is more or less stable. This can be explained by the fact that the surface atoms of the non-Pt metal are dissolved by leaching, leaving only the atoms of the non-Pt metal in the core protected by the Pt shell.

A similar trend was observed during the *in situ* measurements (see Fig. S3.19–S3.22 in SI). Fig. 6 summarises the Pt-edges for Pt/C, Pt–Co/KB and Pt–Ni/KB, and Fig. 7 shows the Co(Ni)-edges for Pt–Co/KB and Pt–Ni/KB.

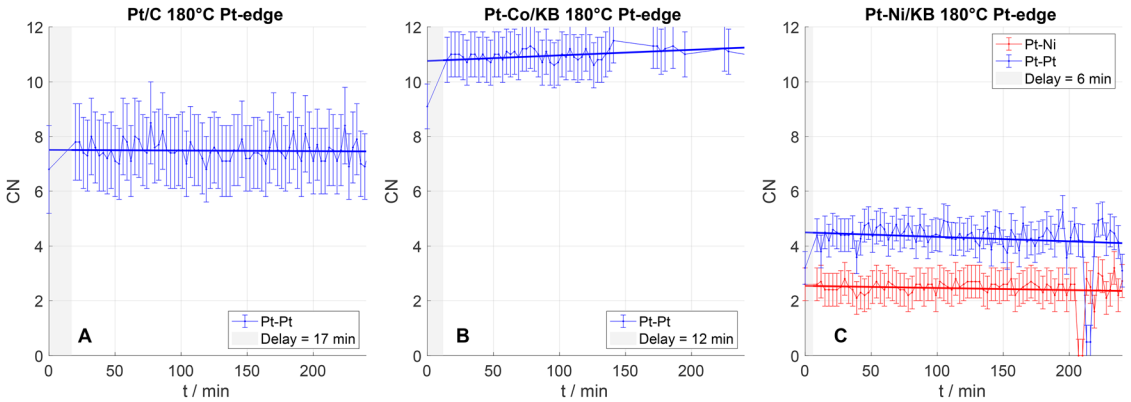

Fig. 6 EXAFS, coordination numbers extracted from Pt-edges, *in situ* XAS in 95 wt% H_3PO_4, 180 °C, GDL 1 mg_{metals} cm^{-2}, notation: Y–X – first central Y atom, second coordinating X atoms, error bars of EXAFS fit (not between replicates).

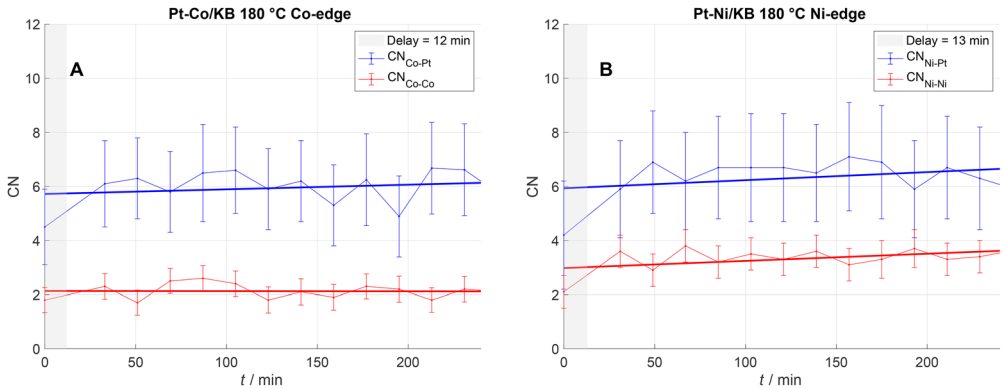

Fig. 7 EXAFS, coordination numbers extracted from Co(Ni)-edges, *in situ* XAS in 95 wt% H_3PO_4, 180 °C, GDL 1 mg_{metals} cm^{-2}, notation: Y–X – first central Y atom, second coordinating X atoms, 7 point moving average, error bars of EXAFS fit (not between replicates).

In situ XAS measurements at the Pt edge show a stable trend in CN_{Pt-Pt} for the Pt/C sample at 180 °C, the coordination number remains approximately constant around 7.5, see Fig. 6A. For the Pt–Co/KB, at the Pt L_3-edge, see Fig. 6B, the EXAFS fitting was restricted to Pt–Pt contributions, since the weaker Pt–Co signals could not be distinguished from the dominant Pt–Pt scattering paths due to the higher scattering amplitude of Pt. Conversely, at the Co and Ni K-edges, both X–Pt and X–X contributions could be fitted, as the strong contrast in backscattering amplitudes makes the heteroatomic coordination more clearly detectable. Pt–Ni/KB shows a stable value of CN_{Pt-Pt} (around 4) and CN_{Pt-Ni} (around 2) in agreement with *ex situ* degradation, see Fig. 6C. Similarly, CN_{Co-Co} and CN_{Co-Pt} values evaluated from Co-edge of Pt–Co/KB remain constant, see Fig. 7A. In contrast, the Ni-edge of Pt–Ni/KB, see Fig. 7B reveals a significant increase in CN_{Ni-Ni} during the 180 °C treatment. This pronounced increase suggests that the remaining Ni atoms become confined within a Ni-rich core.

Finally, Table S3.3 and Fig. S3.23–S3.25 summarises post-mortem XRD of used GDEs used for *in situ* XAS measurements, where growing particle sizes can be seen (of prepared GDE *vs.* pristine catalyst powder).

These measurements demonstrate the feasibility of using the XAS setup for *in situ* experiments. In the future, a similar approach could be employed to investigate catalyst degradation under identical conditions, but simultaneously with catalyst polarisation and ongoing ORR.

3.3 ORR activity of the catalysts in concentrated H_3PO_4 at elevated temperature

Investigation of the catalysts with RDE is typically carried out in aqueous electrolytes,[75,76] but for use in HT-PEMFCs, it is crucial to explore the catalyst's behaviour in concentrated H_3PO_4 at elevated temperatures.[77] For this application it is possible to use a setup with a glassy carbon rotating rod electrode (RRE) that can withstand the highly aggressive environment of concentrated H_3PO_4 at elevated temperature.[78,79]

A representative set of LSV curves for various catalysts and temperatures of 120–180 °C (revolution rate of 2500 rpm) is shown in Fig. 8, and the corresponding Tafel plots are presented in Fig. S4.1, see SI. It is clear, that the j_{lim} generally increases with increasing temperature.

The pristine Pt–Co/KB showed the best ORR activity in aqueous media. It also performs best in the H_3PO_4 environment. Contrary, the lowest ORR activity was observed for Pt–Co/

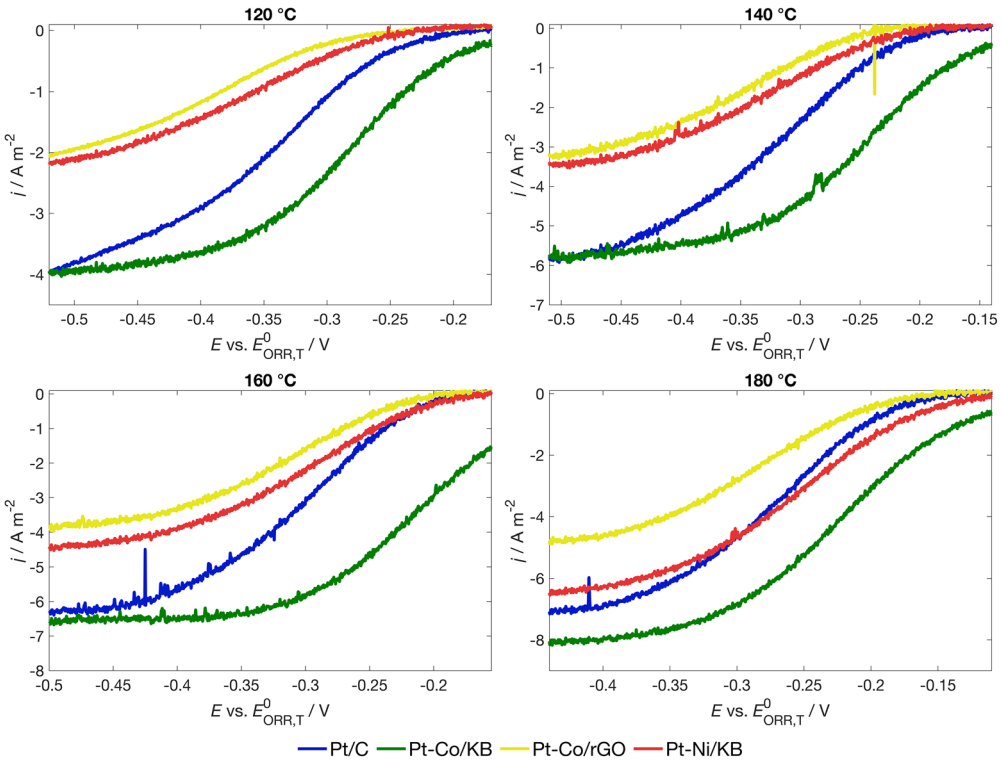

Fig. 8 LSV, RRE using revolution rate 2500 rpm; GC electrode, 10 μg_{metals} cm^{-2}, 97.6 wt% H_3PO_4, 5 mV s^{-1} corrected for background currents and uncompensated resistance, use of corresponding $E_{ORR,g,T}$.

rGO. This can be attributed to an improved stability of the catalyst supported by rGO preventing more significant dealloying of the nanoparticles as discussed previously. A similar behaviour of the same catalyst has also been observed in the literature when used in a HT-PEMFC single-cell cathode.[63]

The obtained ORR LSV data at various temperatures were analysed to obtain the Tafel slope, charge transfer coefficient (α) and exchange current density values (j_{ex}). The results are summarised in Fig. 9 and numerically in Table S4.1, see SI.

Alloy catalysts generally exhibit a lower value of ORR Tafel slope than Pt/C. If the charge transfer coefficient α remained constant within the temperature range, the Tafel slope value would be expected to increase with temperature. In this study, the Tafel slope of all catalysts generally decreases with increasing temperature and approaches values of around −105 mV dec^{-1} at 180 °C, which is comparable to the value observed for ORR on Pt in concentrated H_3PO_4 at 150–180 °C.[77,80]

It should be noted that the measurement itself takes a finite amount of time, during which the catalyst can undergo changes as discussed in the previous section. Additionally, the catalysts are polarised during the experiments, which may affect the kinetics of such transformations. Nevertheless, in these particular experiments, the presence of a significant excess of H_3PO_4 and intensive electrode rotation likely suppress Ostwald ripening by rapidly removing dissolved Pt^{2+} from the diffusion layer and thus minimising redeposition.

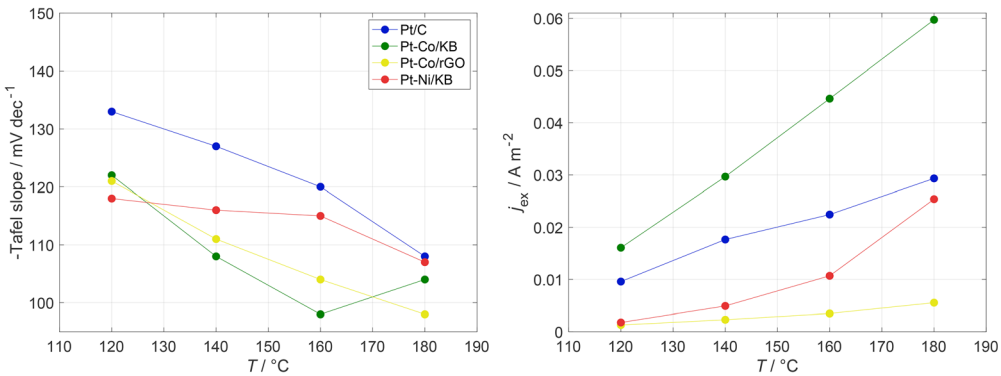

Fig. 9 LSV, and Tafel slopes (left) and exchange current densities (right), RRE using revolution rate 2500 rpm; GC electrode, 10 μg_{metals} cm^{-2}, 97.6 wt% H_3PO_4, 180 °C, 5 mV s^{-1}, corrected for background currents and uncompensated resistance, use of corresponding $E_{ORR,g,T}$.

In the case of pure Pt, a change in Tafel slope is still observed, which may stem from changes in the reaction mechanism, changes in surface energy, or temperature-induced surface restructuring. The behaviour observed for non-Pt components supports previous findings that nearly all non-Pt metals leach out from the Pt surface region where the ORR takes place. This suggests that, temperature-induced modifications (such as a decrease in phosphate coverage, restructuring of surface sites, or changes in surface energy) can significantly impact the reaction kinetics. These effects may act synergistically and could explain the observed decrease in Tafel slopes.

Overall, the convergence of Tafel slope values for all tested catalysts at elevated temperatures implies that the apparent electrochemical behaviour under these conditions is governed more by temperature-driven surface modifications than by the specific alloy composition.

From the j_{ex} values, activation energies were estimated using the methodology described in ref. 60; the values are provided in SI Table S4.2. These values are comparable with those reported in the literature.[81–85] The values differ among the individual alloys; the value of the activation energy follows the increasing trend Pt < Pt–Co < Pt–Ni.

4 Conclusion

In the present work, ORR activity and stability of series of alloy electrocatalysts possessing various carbon supports and alloy compositions (Pt–Co/KB, Pt–Co/rGO and Pt–Ni/KB) was investigated in context of HT-PEMFC (concentrated H_3PO_4 at 140–180 °C) operation and compared to state-of-the-art Pt/C catalyst. In aqueous $HClO_4$ at 25 °C, all three alloy catalysts (pristine and after degradation in concentrated H_3PO_4 at elevated temperatures) delivered higher ORR activity than Pt/C despite the lower Pt content. Stability in HT-PEMFC relevant conditions is governed not only by alloy composition but also by the carbon support. Influence of the support is clearly visible from comparison of Pt–Co/KB and Pt–Co/rGO. While the former undergoes total dealloying and Ostwald ripening, the latter exhibits reasonable Co retention and negligible nanoparticle growth. Focusing on alloy type, Pt–Ni/KB shows suppressed Ostwald ripening and minimal Ni dissolution, which is strong contrast to Pt–Co alloy instability on the same support. On the other hand, dealloying of Pt–Co/KB allows (on short time scale) superior electrocatalytical activity for ORR under HT-PEMFC-relevant conditions.

In summary, the newly developed alloy catalysts achieve Pt/C-level ORR activity at lower Pt loadings, offering a credible route to Pt-lean cathodes. These results suggest that finding suitable combination of carbonaceous support and alloy composition is a key to development of practically useful HT-PEMFC catalyst. To translate these materials' promise into device-level durability, following experiments should focus on long-term polarisation/accelerated stress test campaigns in concentrated H_3PO_4 (140–180 °C), coupled with *operando* structural/composition analyses to relate activity to alloy composition and nanoparticle-size evolution.

Conflicts of interest

There are no conflicts to declare.

List of abbreviations

ECSA	Electrochemically active surface area
EDS	Energy dispersive spectroscopy
EXAFS	Extended X-ray absorption fine structure
FC	Fuel cell
GC	Glassy carbon
GDL	Gas diffusion layer
GO	Graphene oxide
HT	High temperature
ICP-OES	Inductively coupled plasma with optical emission spectroscopy
K–L	Koutecky–Levich
KB	Ketjen black
LSV	Linear sweep voltammetry
LT	Low temperature
MSE	Mercury-mercurous sulphate electrode (saturated)
ORR	Oxygen reduction reaction
PBI	Polybenzimidazole
PEMFC	Proton-exchange membrane fuel cell
PTFE	Polytetrafluorethylene
RDE	Rotating disk electrode
rGO	Reduced graphene oxide
RHE	Reversible hydrogen electrode
RRE	Rotating rod disk electrode
TEM	Transmission electron microscopy
XAS	X-ray absorption spectroscopy
XRD	X-ray diffraction
XRF	X-ray fluorescence
XPS	X-ray photoelectron spectroscopy

Data availability

The data supporting this article have been included as part of the supplementary information (SI). Supplementary information is available at DOI: https://doi.org/10.1039/d5ey00279f.

Data for this article, including structured raw data accompanied with data description are available at Zenodo at https://doi.org/10.5281/zenodo.17131699.

Acknowledgements

This work was supported from the grants of Specific university research – grants no. A2_FCHT_2023_039, A2_FCHT_2024_016, A2_FCHT_2025_030 of University of Chemistry and Technology, Prague; and by Czech Science Foundation Grant No. 22-23668K. Financial support by the project ''The Energy Conversion and Storage'', funded as project no. CZ.02.01.01/00/22_008/0004617 by Programme Johannes Amos Comenius, call Excellent Research is also gratefully acknowledged. We acknowledge DESY (Hamburg, Germany), a member of the Helmholtz

Association HGF, for the provision of experimental facilities. Parts of this research were carried out at PETRA III, and we would like to thank Wolfgang Caliebe and Edmund Welter for their assistance in using the P64 and P65 beamlines. Beamtime was allocated for proposals I-20230896, I-20240368, I-20221072, and I-20230933. B. F. G. and C. R. acknowledges funding from the Federal Ministry of Education and Research (BMBF) through the projects Live XAS (Grant 05K22WC1) and HighHy (Grant 03SF0689B). C. M. S. L. and C. R. acknowledge the funding granted by the Deutsche Forschungsgemeinschaft (DFG, German Research Foundation) – DFG priority program SPP 2370 (RO 2454/26-1). The authors would like to acknowledge the Slovenian Research and Innovation Agency (ARIS) programs P2-0393 and I0-0003; the projects NC-0016, N2-0257, J7-4637 and N2-0385; and NATO Science for Peace and Security Program (Grant G6230). The authors also acknowledge partial support from the Republic of Slovenia, Ministry of Higher Education, Science and Innovation, and from the European Union—NextGenerationEU in the framework of the project HyBReED, which is part of the Slovenian Recovery and Resilience Plan. Views and opinions expressed are, however, those of the authors only and do not necessarily reflect those of the Republic of Slovenia, the Ministry of Higher Education, the European Union or the European Commission. Neither the Republic of Slovenia, the Ministry of Higher Education, Science and Innovation, the European Union, nor the European Commission can be held responsible for them.

References

1 A. Midilli, *et al.*, On hydrogen and hydrogen energy strategies: I: current status and needs, *Renewable Sustainable Energy Rev.*, 2005, **9**(3), 255–271.
2 M. Temiz and I. Dincer, Development of solar and wind based hydrogen energy systems for sustainable communities, *Energy Convers. Manage.*, 2022, **269**, 116090.
3 J.-H. Wee, Applications of proton exchange membrane fuel cell systems, *Renewable Sustainable Energy Rev.*, 2007, **11**(8), 1720–1738.
4 T. Yoshida and K. Kojima, Toyota MIRAI fuel cell vehicle and progress toward a future hydrogen society, *Electrochem. Soc. Interface*, 2015, **24**(2), 45.
5 Q. Li, *et al.*, *High temperature polymer electrolyte membrane fuel cells*, Springer, Cham Heidelberg New York Dordrecht London, 2016, p. 545.
6 A. Bergmann, D. Gerteisen and T. Kurz, Modelling of CO poisoning and its dynamics in HTPEM fuel cells, *Fuel Cells*, 2010, **10**(2), 278–287.
7 S. Mekhilef, R. Saidur and A. Safari, Comparative study of different fuel cell technologies, *Renewable Sustainable Energy Rev.*, 2012, **16**(1), 981–989.
8 J. Zhang, *et al.*, Advancement toward Polymer Electrolyte Membrane Fuel Cells at Elevated Temperatures, *Research*, 2020, **2020**, 9089405.
9 I. I. Ponomarev, *et al.*, Cardo Polybenzimidazole (PBI-O-PhT) Based Membrane Reinforced with m-Polybenzimidazole Electrospun Nanofiber Mat for HT-PEM Fuel Cell Applications, *Membranes*, 2022, **12**(10), 956.
10 R. Taccani, T. Chinese and M. Boaro, Effect of accelerated ageing tests on PBI HTPEM fuel cells performance degradation, *Int. J. Hydrogen Energy*, 2017, **42**(3), 1875–1883.
11 C. Hasiotis, *et al.*, Development and characterization of acid-doped polybenzimidazole/sulfonated polysulfone blend polymer electrolytes for fuel cells, *J. Electrochem. Soc.*, 2001, **148**(5), A513.
12 L. Qingfeng, H. A. Hjuler and N. Bjerrum, Phosphoric acid doped polybenzimidazole membranes: physiochemical characterization and fuel cell applications, *J. Appl. Electrochem.*, 2001, **31**, 773–779.
13 L. Qingfeng, H. A. Hjuler and N. J. Bjerrum, Oxygen reduction on carbon supported platinum catalysts in high temperature polymer electrolytes, *Electrochim. Acta*, 2000, **45**(25–26), 4219–4226.
14 J. Zhang, *et al.*, High temperature PEM fuel cells, *J. Power Sources*, 2006, **160**(2), 872–891.
15 K. Hooshyari, *et al.*, A review of recent developments and advanced applications of high-temperature polymer electrolyte membranes for PEM fuel cells, *Energies*, 2021, **14**(17), 5440.
16 E. Romero-Pascual and J. Soler, Modelling of an HTPEM-based micro-combined heat and power fuel cell system with methanol, *Int. J. Hydrogen Energy*, 2014, **39**(8), 4053–4059.
17 B. Ferreira Gomes Lobo, *et al.*, Following Adsorbed Intermediates on a Platinum Gas Diffusion Electrode in H_3PO_3-Containing Electrolytes Using In Situ X-ray Absorption Spectroscopy, *ACS Catal.*, 2022, **12**(18), 11472–11484.
18 M. Prokop, *et al.*, H3PO3 electrochemical behaviour on a bulk Pt electrode: adsorption and oxidation kinetics, *Electrochim. Acta*, 2016, **212**, 465–472.
19 M. Prokop, *et al.*, High-temperature PEM fuel cell electrode catalyst layers part 1: Microstructure reconstructed using FIB-SEM tomography and its calculated effective transport properties, *Electrochim. Acta*, 2022, **413**, 140133.
20 M. Prokop, *et al.*, High-temperature PEM fuel cell electrode catalyst layers Part 2: Experimental validation of its effective transport properties, *Electrochim. Acta*, 2022, **413**, 140121.
21 M. Prokop, M. Drakselova and K. Bouzek, Review of the experimental study and prediction of Pt-based catalyst degradation during PEM fuel cell operation, *Curr. Opin. Electrochem.*, 2020, **20**, 20–27.
22 A. Hrnjic, *et al.*, Observing, tracking and analysing electrochemically induced atomic-scale structural changes of an individual Pt-Co nanoparticle as a fuel cell electrocatalyst by combining modified floating electrode and identical location electron microscopy, *Electrochim. Acta*, 2021, **388**, 138513.
23 A. Appleby, Oxygen Reduction on Oxide-Free Platinum in 85% Orthophosphoric Acid: Temperature and Impurity Dependence, *J. Electrochem. Soc.*, 1970, **117**(3), 328.
24 Y.-J. Deng, *et al.*, On the oxygen reduction reaction in phosphoric acid electrolyte: Evidence of significantly

increased inhibition at steady state conditions, *Electrochim. Acta*, 2016, **204**, 78–83.
25 P. Schneider, *et al.*, Impact of platinum loading and layer thickness on cathode catalyst degradation in PEM fuel cells, *J. Electrochem. Soc.*, 2023, **170**(2), 024506.
26 J. K. Nørskov, *et al.*, Origin of the overpotential for oxygen reduction at a fuel-cell cathode, *J. Phys. Chem. B*, 2004, **108**(46), 17886–17892.
27 R. M. Darling and J. P. Meyers, Kinetic model of platinum dissolution in PEMFCs, *J. Electrochem. Soc.*, 2003, **150**(11), A1523.
28 Y. Shao, G. Yin and Y. Gao, Understanding and approaches for the durability issues of Pt-based catalysts for PEM fuel cell, *J. Power Sources*, 2007, **171**(2), 558–566.
29 V. R. Stamenkovic, *et al.*, Energy and fuels from electrochemical interfaces, *Nat. Mater.*, 2017, **16**(1), 57–69.
30 H. Chen, *et al.*, Pt–Co Electrocatalysts: Syntheses, Morphologies, and Applications, *Small*, 2022, **18**(40), 2204100.
31 H. R. Colón-Mercado and B. N. Popov, Stability of platinum based alloy cathode catalysts in PEM fuel cells, *J. Power Sources*, 2006, **155**(2), 253–263.
32 M. Gatalo, *et al.*, Importance of Chemical Activation and the Effect of Low Operation Voltage on the Performance of Pt-Alloy Fuel Cell Electrocatalysts, *ACS Appl. Energy Mater.*, 2022, **5**(7), 8862–8877.
33 P. A. Heizmann, *et al.*, *PtCo/C catalysts with narrow particle size distribution improve high current density operation in PEM fuel cells*, 2022.
34 H. Lin, *et al.*, High-Temperature Rotating Disk Electrode Study of Platinum Bimetallic Catalysts in Phosphoric Acid, *ACS Catal.*, 2023, **13**(8), 5635–5642.
35 M. Gatalo, *et al.*, Comparison of Pt–Cu/C with benchmark Pt–Co/C: metal dissolution and their surface interactions, *ACS Appl. Energy Mater.*, 2019, **2**(5), 3131–3141.
36 C. Grimmer, *et al.*, Manufacturing and Stabilization of PtCo/C Cocatalysts for PEM Fuel Cells, *ECS Trans.*, 2013, **58**(1), 753.
37 R. Muntean, *et al.*, Studies on Pulse Electrodeposition of Pt-Ni binary Alloy For Electrochemical Cell Applications, *IOP Conference Series: Materials Science and Engineering*, IOP Publishing, 2018.
38 T. Priamushko, R. Guillet-Nicolas and F. Kleitz, Mesoporous nanocast electrocatalysts for oxygen reduction and oxygen evolution reactions, *Inorganics*, 2019, **7**(8), 98.
39 L. J. Moriau, *et al.*, Resolving the nanoparticles' structure-property relationships at the atomic level: a study of Pt-based electrocatalysts, *iScience*, 2021, **24**(2), 102102.
40 J. Müller-Hülstede, *et al.*, Towards the Reduction of Pt Loading in High Temperature Proton Exchange Membrane Fuel Cells–Effect of Fe–N–C in Pt-Alloy Cathodes, *ChemSusChem*, 2023, **16**(5), e202202046.
41 M. Prokop, *et al.*, Degradation kinetics of Pt during high-temperature PEM fuel cell operation Part III: Voltage-dependent Pt degradation rate in single-cell experiments, *Electrochim. Acta*, 2020, **363**, 137165.
42 M. Prokop, *et al.*, Degradation kinetics of Pt during high-temperature PEM fuel cell operation part II: dissolution kinetics of Pt incorporated in a catalyst layer of a gas-diffusion electrode, *Electrochim. Acta*, 2020, **333**, 135509.
43 M. Prokop, *et al.*, Degradation kinetics of Pt during high-temperature PEM fuel cell operation part I: Kinetics of Pt surface oxidation and dissolution in concentrated H3PO4 electrolyte at elevated temperatures, *Electrochim. Acta*, 2019, **313**, 352–366.
44 B. F. Gomes, *et al.*, Effect of phosphoric acid purity on the electrochemically active surface area of Pt-based electrodes, *J. Electroanal. Chem.*, 2022, **918**, 116450.
45 M. Prokop, T. Bystron and K. Bouzek, Electrochemistry of Phosphorous and Hypophosphorous Acid on a Pt electrode, *Electrochim. Acta*, 2015, **160**, 214–218.
46 Y. Hu, *et al.*, Catalyst evaluation for oxygen reduction reaction in concentrated phosphoric acid at elevated temperatures, *J. Power Sources*, 2018, **375**, 77–81.
47 Y. Li, *et al.*, Influence of phosphoric anions on oxygen reduction reaction activity of platinum, and strategies to inhibit phosphoric anion adsorption, *Chin. J. Catal.*, 2016, **37**(7), 1134–1141.
48 M. Luo and M. T. Koper, A kinetic descriptor for the electrolyte effect on the oxygen reduction kinetics on Pt (111), *Nat. Catal.*, 2022, **5**(7), 615–623.
49 C. Wang and J. S. Spendelow, Recent developments in Pt–Co catalysts for proton-exchange membrane fuel cells, *Curr. Opin. Electrochem.*, 2021, **28**, 100715.
50 P. A. Heizmann, *et al.*, Alternative and facile production pathway towards obtaining high surface area PtCo/C intermetallic catalysts for improved PEM fuel cell performance, *RSC Adv.*, 2023, **13**(7), 4601–4611.
51 T. Đukić, *et al.*, Stability challenges of carbon-supported Pt-nanoalloys as fuel cell oxygen reduction reaction electrocatalysts, *Chem. Commun.*, 2022, **58**(100), 13832–13854.
52 T. Đukić, *et al.*, Understanding the crucial significance of the temperature and potential window on the stability of carbon supported Pt-alloy nanoparticles as oxygen reduction reaction electrocatalysts, *ACS Catal.*, 2021, **12**(1), 101–115.
53 L. Pavko, *et al.*, Graphene-Derived Carbon Support Boosts Proton Exchange Membrane Fuel Cell Catalyst Stability, *ACS Catal.*, 2022, **12**(15), 9540–9548.
54 F. R. Nikkuni, *et al.*, Accelerated degradation of Pt3Co/C and Pt/C electrocatalysts studied by identical-location transmission electron microscopy in polymer electrolyte environment, *Appl. Catal., B*, 2015, **176**, 486–499.
55 L. Pavko, *et al.*, Correlating oxygen functionalities and electrochemical durability of carbon supports for electrocatalysts, *Carbon*, 2023, **215**, 118458.
56 L. Pavko, *et al.*, Toward the continuous production of multigram quantities of highly uniform supported metallic nanoparticles and their application for synthesis of superior intermetallic Pt-Alloy ORR electrocatalysts, *ACS Appl. Energy Mater.*, 2021, **4**(12), 13819–13829.
57 N. Sugishima, J. T. Hinatsu and F. R. Foulkes, Phosphorous acid impurities in phosphoric acid fuel cell electrolytes: I. Voltammetric study of impurity formation, *J. Electrochem. Soc.*, 1994, **141**(12), 3325.

58 D. I. MacDonald and J. R. Boyack, Density, electrical conductivity, and vapor pressure of concentrated phosphoric acid, *J. Chem. Eng. Data*, 1969, **14**(3), 380–384.
59 X. Jiang, *et al.*, Density, viscosity, and thermal conductivity of electronic grade phosphoric acid, *J. Chem. Eng. Data*, 2011, **56**(2), 205–211.
60 J. Buriánek, T. Bystron and K. Bouzek, Methodology of evaluating the activation energy of oxygen reduction reaction on Pt-based electrodes, *J. Electroanal. Chem.*, 2025, 119418.
61 E. Zhang, *et al.*, NMR analysis of phosphoric acid distribution in porous fuel cell catalysts, *Chem. Commun.*, 2021, **57**(20), 2547–2550.
62 Z. Liu, *et al.*, A supercapacitor with ultrahigh volumetric capacitance produced by self-assembly of reduced graphene oxide through phosphoric acid treatment, *J. Mater. Chem. A*, 2020, **8**(36), 18933–18944.
63 V. Domin, *et al.*, Performance and stability of PtCo alloy catalysts in high-temperature polymer electrolyte membrane fuel cells, *Electrochim. Acta*, 2025, 146707.
64 Y. Chen, *et al.*, Ni–Pt core–shell nanoparticles as oxygen reduction electrocatalysts: effect of Pt shell coverage, *J. Phys. Chem. C*, 2011, **115**(49), 24073–24079.
65 A. A. Popov, *et al.*, X-ray diffraction reinvestigation of the Ni-Pt phase diagram, *J. Alloys Compd.*, 2022, **891**, 161974.
66 Y. Chen, *et al.*, Ni@ Pt core–shell nanoparticles: synthesis, structural and electrochemical properties, *J. Phys. Chem. C*, 2008, **112**(5), 1645–1649.
67 J. Ding, *et al.*, Morphology and phase controlled construction of Pt–Ni nanostructures for efficient electrocatalysis, *Nano Lett.*, 2016, **16**(4), 2762–2767.
68 Y. Hu, *et al.*, Effects of structure, composition, and carbon support properties on the electrocatalytic activity of Pt-Ni-graphene nanocatalysts for the methanol oxidation, *Appl. Catal., B*, 2012, **111**, 208–217.
69 E. Antolini, Alloy vs. intermetallic compounds: Effect of the ordering on the electrocatalytic activity for oxygen reduction and the stability of low temperature fuel cell catalysts, *Appl. Catal., B*, 2017, **217**, 201–213.
70 G. Wang, *et al.*, Quantitative prediction of surface segregation in bimetallic Pt–M alloy nanoparticles (M = Ni, Re, Mo), *Prog. Surf. Sci.*, 2005, **79**(1), 28–45.
71 B. Mun, *et al.*, The study of surface segregation, structure, and valence band density of states of Pt 3 Ni (100),(110), and (111) crystals, *Surf. Rev. Lett.*, 2006, **13**(05), 697–702.
72 V. Stamenković, *et al.*, Surface composition effects in electrocatalysis: Kinetics of oxygen reduction on well-defined Pt3Ni and Pt3Co alloy surfaces, *J. Phys. Chem. B*, 2002, **106**(46), 11970–11979.
73 B. Patrick, *et al.*, Atomic structure and composition of ''Pt3Co'' nanocatalysts in fuel cells: an aberration-corrected STEM HAADF study, *Chem. Mater.*, 2013, **25**(4), 530–535.
74 J. C. Slater, Atomic radii in crystals, *J. Chem. Phys.*, 1964, **41**(10), 3199–3204.
75 R. Halseid, T. Bystroň and R. Tunold, Oxygen reduction on platinum in aqueous sulphuric acid in the presence of ammonium, *Electrochim. Acta*, 2006, **51**(13), 2737–2742.
76 P. Wongbua-ngam, *et al.*, Model interpretation of electrochemical behavior of Pt/H2SO4 interface over both the hydrogen oxidation and oxide formation regions, *Int. J. Hydrogen Energy*, 2019, **44**(23), 12108–12117.
77 S. Clouser, J. Huang and E. Yeager, Temperature dependence of the Tafel slope for oxygen reduction on platinum in concentrated phosphoric acid, *J. Appl. Electrochem.*, 1993, **23**, 597–605.
78 M. Prokop, *et al.*, A rotating rod electrode disk as an alternative to the rotating disk electrode for medium-temperature electrolytes, Part I: The effect of the absence of cylindrical insulation, *Electrochim. Acta*, 2017, **245**, 634–642.
79 M. Prokop, *et al.*, A rotating rod electrode disk as an alternative to the rotating disk electrode for medium-temperature electrolytes, Part II: An example of the application in an investigation of the oxygen reduction reaction on a Pt/C catalyst by the thin film method in hot concentrated H3PO4, *Electrochim. Acta*, 2017, **245**, 597–606.
80 Z. Liu, *et al.*, Study of the oxygen reduction reaction (ORR) at Pt interfaced with phosphoric acid doped polybenzimidazole at elevated temperature and low relative humidity, *Electrochim. Acta*, 2006, **51**(19), 3914–3923.
81 N. Wakabayashi, *et al.*, Temperature-dependence of oxygen reduction activity at a platinum electrode in an acidic electrolyte solution investigated with a channel flow double electrode, *J. Electroanal. Chem.*, 2005, **574**(2), 339–346.
82 A. B. Anderson, *et al.*, Activation energies for oxygen reduction on platinum alloys: Theory and experiment, *J. Phys. Chem. B*, 2005, **109**(3), 1198–1203.
83 A. B. Anderson and T. V. Albu, Catalytic effect of platinum on oxygen reduction an ab initio model including electrode potential dependence, *J. Electrochem. Soc.*, 2000, **147**(11), 4229.
84 A. S. Haile, W. Yohannes and Y. S. Mekonnen, Oxygen reduction reaction on Pt-skin Pt 3 V (111) fuel cell cathode: a density functional theory study, *RSC Adv.*, 2020, **10**(46), 27346–27356.
85 N. Wakabayashi, *et al.*, Temperature dependence of oxygen reduction activity at Pt–Fe, Pt–Co, and Pt–Ni alloy electrodes, *J. Phys. Chem. B*, 2005, **109**(12), 5836–5841.